Available online at www.sciencedirect.com
SCIENCE DIRECT®
Computers & Fluids 35 (2006) 304–325
computers & fluids
www.elsevier.com/locate/compfluid

A viscous inverse method for aerodynamic design

Michele Ferlauto *, Roberto Marsilio

Dipartimento di Ingegneria Aeronautica e Spaziale, Politecnico di Torino, Corso Duca degli Abruzzi 24, 10129 Torino, Italy

Received 24 September 2003; received in revised form 4 May 2004; accepted 4 January 2005
Available online 21 April 2005

Abstract

A numerical technique to solve two-dimensional inverse problems that arise in aerodynamic design is presented. The approach, which is well-established for inviscid, rotational flows, is here extended to the viscous case. Two-dimensional and axisymmetric configurations are here considered. The solution of the inverse problem is given as the steady state of an ideal transient during which the flowfield assesses itself to the boundary conditions by changing the boundary contour. Comparisons with theoretical and experimental results are used to validate the numerical procedure.

1. Introduction

Aerodynamic design consists of finding the most convenient shape of a fluid-immersed body to obtain the expected aerodynamic performances. There is a certain freedom in approaching aerodynamic design. The most-followed methods iterate on a sequence of *direct problems*. In computational fluid dynamics (CFD) the automation of this procedure is known as the classical *shape optimization* [1]. The design problem mathematically can also be formulated as an indirect or, *inverse problem*, where the independent variables are now the flow variables and the geometry is sought from a pressure or Mach number distribution that meets some performance requirements.

* Corresponding author. Tel.: +39 11 5646834; fax: +39 11 5646899.
E-mail addresses: michele.ferlauto@polito.it (M. Ferlauto), roberto.marsilio@polito.it (R. Marsilio).

0045-7930/$ - see front matter © 2005 Elsevier Ltd. All rights reserved.
doi:10.1016/j.compfluid.2005.01.003

By iterating on direct problems it is easier to satisfy geometrical constraints, while design constraints that involve the control of a flow feature are more effectively enforced by inverse procedures. A typical inverse problem solves for the geometry that realizes a specified wall pressure distribution. By a proper selection of this distribution one can, for instance, control the wall pressure gradient to avoid the flow separation [2], or to obtain shock-free flowfields [3], or to reduce aerodynamic noise [4]. In a multidisciplinary design environment the solution of an inverse problem should be considered an alternative approach of fulfilling various and heterogeneous requirements and constraints dictated by different disciplines. Optimization techniques based on the adjoint method have recently been adopted to drive inverse problems towards the maximization or minimization of target functionals [2].

First approaches to the solution of inverse problems were based on the potential flow theory and conformal mapping techniques [5–8]. Other methods replace the body surface with singularity distributions while also trying to simulate boundary layer blockage [9]. Several examples of inverse problem solution methodologies are shown in Elizarov et al. [10] and in the AGARD-R-780 volume [11]. Many of these solution techniques do not deal with rotational flows or shocks and often cannot be extend to three-dimensional case. A generalisable way of solving inverse problems simulates a transient during which the flowfield accommodates itself to the design data, which are prescribed at walls as boundary conditions [12]. These walls are modelled as flexible and impermeable surfaces [12–14] either the wall is permeable and a transpiration velocity model is adopted [15].

The main advantage of this approach is that any well-proven analysis code, able to deal with moving grids, can be adopted with some alterations of the boundary condition enforcement. Using Euler solvers, the methodology has been extended to three-dimensional compressible [15,16] and incompressible flows [17]. In Ref. [18] an inverse problem is solved for the simultaneous design of engine components interacting with the external flow.

Various extensions has been proposed to take into account viscous effects, either by introducing a boundary layer approximation [9,19], or by coupling a Navier–Stokes direct solver to an Euler inverse solver [20].

In the present paper a Navier–Stokes inverse solver is derived as a natural extension of the approach of Ref. [12] to viscous inverse problems. As an initial step, the study is limited to two-dimensional and axisymmetric flows, but the procedure can be straightly applied to three-dimensional cases. The design case of wing or blade profiles is also feasible, but it is not considered here, since it merits a more extended discussion about the way of formulating the inverse problem and to satisfy or to overcome the related well-posedness issues [3,8,13,21].

The plan of the work is as follows: the mathematical model and the numerical technique are explained in the context of a characteristic-based method in the first sections. Then the equation of motion of impermeable surfaces is derived for the two-dimensional and axisymmetric cases; the extension of the numerical procedure to viscous flows is explained and, finally, the accuracy of the method is studied through comparisons with theoretical and experimental results.

2. Governing equations

Compressible viscous flows are governed by the Navier–Stokes equations. This set of equations may be written in a compact integral conservative form as:

$$\frac{\partial}{\partial t}\int_{\mathscr{V}} \boldsymbol{W}\,\mathrm{d}\mathscr{V} + \int_{\mathscr{S}} (\boldsymbol{F}_\mathrm{I} - \boldsymbol{F}_\mathrm{V})\cdot \boldsymbol{n}\,\mathrm{d}\mathscr{S} = 0 \tag{1}$$

where $\mathscr{V}$ represents an arbitrary volume enclosed in a surface $\mathscr{S}$. System (1) is reduced to non-dimensional form with the help of the following reference values: L for length, ρ_∞ for density, T_∞ for temperature, $\sqrt{RT_\infty}$ for velocity, RT_∞ for energy per unit mass and μ_∞ for viscosity. In particular, $\boldsymbol{W}$ is the vector of conservative variables while tensors $\boldsymbol{F}_\mathrm{I}$, $\boldsymbol{F}_\mathrm{V}$ contain the inviscid and the viscous fluxes, respectively.

$$\begin{aligned}
\boldsymbol{W} &= \{\rho, \rho\boldsymbol{q}, E\}^\mathrm{T} \\
\boldsymbol{F}_\mathrm{I} &= \{\rho\boldsymbol{q}, p\boldsymbol{I} + \rho\boldsymbol{q}\otimes\boldsymbol{q}, (E+p)\boldsymbol{q}\}^\mathrm{T} \\
\boldsymbol{F}_\mathrm{V} &= \frac{\sqrt{\gamma}M_\infty}{Re_\infty}\{0, \boldsymbol{\tau}, \kappa\nabla T + \boldsymbol{\tau}\cdot\boldsymbol{q}\}^\mathrm{T}
\end{aligned} \tag{2}$$

Quantities ρ, p, T, $\boldsymbol{q} = \{u, v\}^\mathrm{T}$ and R are the local density, the pressure, the temperature, the velocity vector and the gas constant, respectively. E represents the total energy per unit volume:

$$E = \rho\left(e + \frac{q^2}{2}\right) \tag{3}$$

where e is the internal energy per unit mass, M_∞ and Re_∞ are the free-stream Mach number and the Reynolds number, γ is the ratio of the specific heats, and finally $\boldsymbol{I}$ is the unit matrix. The viscous stresses $\boldsymbol{\tau}$ are contained in tensor, given by:

$$\tau_{ij} = \mu\left[\frac{\partial q_j}{\partial x_i} + \frac{\partial q_i}{\partial x_j} - \frac{2}{3}(\nabla\cdot\boldsymbol{q})\delta_{ij}\right] \tag{4}$$

The thermal conductivity κ is calculated in non-dimensional form as

$$\kappa = \frac{\gamma}{\gamma - 1}\left(\frac{\mu}{\mathrm{Pr}}\right) \tag{5}$$

where Pr is the Prandtl number. The viscosity μ is computed via Sutherland's law and the perfect gas relationship $p = \rho T$ completes the set of equations.

A two-dimensional/axisymmetric formulation of system (1) is here solved using a finite volume technique by discretizing the (x, y) plane by means of quadrilateral cells [22] on time-varying computational domains.

In case of an axisymmetric flow, system (1) may be reduced to a two-dimensional form, where the two independent variables are the axial direction x and the radial direction y. The discretized system on the i,j cell at the $k+1$ integration step takes the following form:

$$\boldsymbol{W}_{i,j}^{k+1} = \boldsymbol{W}_{i,j}^{k} - \frac{\Delta t}{A y_\mathrm{c}}\left[\sum_{l=1}^{4}(\boldsymbol{F}_\mathrm{I} - \boldsymbol{F}_\mathrm{V})_l s_l y_l - \boldsymbol{H}_\mathrm{I} - \boldsymbol{H}_\mathrm{V}\right] \tag{6}$$

Source terms $\boldsymbol{H}_\mathrm{I}$ and $\boldsymbol{H}_\mathrm{V}$ account for the effects of pressure and shear stress tensor on lateral surfaces of the elementary volume:

$$\boldsymbol{H}_{\mathrm{I}} = \{0, 0, pA, 0\}^{\mathrm{T}}, \qquad \boldsymbol{H}_{\mathrm{V}} = \left\{0, 0, -\frac{\sqrt{\gamma}M_{\infty}}{Re_{\infty}}\tau_{\theta\theta}A, 0\right\}^{\mathrm{T}} \tag{7}$$

with

$$\tau_{\theta\theta} = \mu\left[\frac{4}{3}\frac{v}{y_{\mathrm{c}}} - \frac{2}{3}\left(\frac{\partial u}{\partial x} + \frac{\partial v}{\partial y}\right)\right] \tag{8}$$

where u and v are the axial and the radial components of the velocity, respectively. The two-dimensional representation of an elementary control volume is shown in Fig. 1. Symbol A represents the cell surface, s_l are its sides ($l = 1, 2, 3, 4$), y_l are the average distances of the sides from the symmetry axis and y_{c} is the distance of the cell center from the symmetry axis.

The integration in time is carried out according to a two-step Godunov scheme. At the *predictor* step, a standard first order flux difference splitting (FDS) scheme is used [23]: the conservative variables $\boldsymbol{W}$ are assumed as an averaged, constant value inside each cell. The fluxes $\boldsymbol{F}_{\mathrm{I}}$ are evaluated by solving the Riemann's problems pertinent to the discontinuities that take place at the interfaces of the cells. At the *corrector* level, the second order of accuracy is achieved by assuming a linear, instead of constant, behavior of the conservative variables inside the cells, according to an essentially non-oscillatory (ENO) scheme [24]. The resulting scheme is second order accurate in both time and space. The velocity and temperature gradients that are required to evaluate the viscous fluxes $\boldsymbol{F}_{\mathrm{V}}$ in correspondence to the lateral surface are computed using a integral technique that utilizes central differences and applies Gauss's theorem.

2.1. Boundary conditions

The computational domain is bounded by artificial (i.e. far field boundaries) and physical contours (i.e. impermeable walls), which can be solid, as in the direct problem, flexible, as in the inverse problem, or partly solid and partly flexible. The boundary condition (BC) enforcement follows the guidelines given in Poinsot and Lele [25]. To the conditions corresponding to inviscid flows, supplementary relations, the *viscous conditions*, are added, to complete the set of boundary conditions needed by Navier–Stokes equations. This approach also ensures that Navier–Stokes equations relax smoothly to Euler equations when the viscosity goes to zero. The unconventional

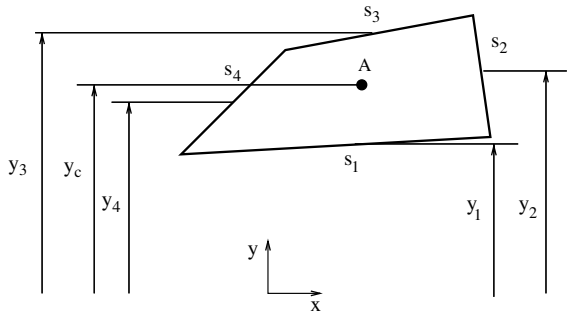

Fig. 1. The finite volume in the axisymmetric case.

part of the boundary condition enforcement is the moving wall BC which is therefore discussed deeply in next section.

2.1.1. Moving wall boundary

When solving the inverse problem, walls on which a flow variable, e.g. the pressure, is imposed, are treated as flexible and impermeable surfaces whose motion is tracked in time until a steady state is reached. In inviscid flows, the velocity vector must be tangent to the wall surface, which is therefore a flow surface and, *it will move materially within the fluid*. These considerations are still valid for viscous flows, but the set of boundary conditions must be completed with the additional viscous relations.

Let us consider a Cartesian coordinate system (x, y). A generic surface moving in time can be represented, for example, by equation $y = \beta(x, t)$. Without any loss of generality, let us also assume that $\beta(x, 0) = 0$. Thanks to the change of variable $\mathscr{B} = y - \beta$ the surface is now defined by the manifold

$$\mathscr{B}(x, y, t) = 0 \tag{9}$$

This manifold moves materially within the fluid, that is,

$$\frac{\partial \mathscr{B}}{\partial t} + \boldsymbol{q} \cdot \nabla \mathscr{B} = 0 \tag{10}$$

or

$$\frac{\partial \beta}{\partial t} = v - u \frac{\partial \beta}{\partial x} \tag{11}$$

The flow velocity $\boldsymbol{q}$ at boundary is obtained by imposing the target pressure on the moving wall and solving the related Riemann problem [12,13,18]. For convenience, when imposing boundary conditions, the flow velocity is expressed both in a local frame of reference $\boldsymbol{q} = \tilde{u}\boldsymbol{n} + \tilde{v}\boldsymbol{\tau}$, where $\boldsymbol{n}$, $\boldsymbol{\tau}$ are the unit vectors normal and tangential to the boundary contour respectively, and in Cartesian coordinates $\boldsymbol{q} = u\boldsymbol{i} + v\boldsymbol{j}$. For example, by using the approach of Ref. [23] to approximate the solution of the Riemann problem, we have

$$\tilde{u} = \frac{2}{\gamma - 1}\left(\sqrt{\gamma p_{\mathrm{w}}(x)^{\frac{\gamma-1}{\gamma}} \mathrm{e}^{\frac{S_{\mathrm{b}}}{\gamma}}} - a_{\mathrm{b}}\right) + \tilde{u}_{\mathrm{b}} \tag{12}$$

where subscript b refers to the ENO reconstruction of the flow state close to the boundary, a is the sound speed, S is entropy and $p_{\mathrm{w}}(x)$ the prescribed wall pressure distribution. It will be shown that the tangential component $\tilde{v}$ does not enter directly in the final expression for b_t. Nevertheless, we can consider $\tilde{v}$ as known from the slip or no-slip condition. In conclusion, $q = \tilde{u}\boldsymbol{n} + \tilde{v}\boldsymbol{\tau}$ is known at the boundary, so that the wall velocity $\partial\beta/\partial t$ can be deduced from (11). The latter is then integrated in time to find the new wall shape. In this context, the no-through-flow condition represents a kinematic constraint from which the motion of the wall surface is derived. The grid is adjusted to fit the updated wall geometry at each time step.

As an example, let us consider a channel that, in a Cartesian frame of reference (x, y) is bound by two inlet and exit permeable boundaries $x = x_{\mathrm{in}}$, $x = x_{\mathrm{ou}}$ and by two impermeable flexible walls

$y = b(x,t)$, $y = c(x,t)$. A boundary fitted grid can be defined by the ξ = constant, η = constant coordinate lines of the frame of reference ξ, η defined by the mapping:

$$\xi = \frac{x - x_{\text{in}}}{x_{\text{ou}} - x_{\text{in}}}, \qquad \eta = \frac{y - b(x,t)}{c(x,t) - b(x,t)} \tag{13}$$

The impermeability of the walls is therefore expressed by the kinematic conditions:

$$\frac{\partial b}{\partial t} = v - u\frac{\partial b}{\partial x}, \qquad \frac{\partial c}{\partial t} = v - u\frac{\partial c}{\partial x} \tag{14}$$

Once $\partial b/\partial x$ and $\partial c/\partial x$ are approximated by finite differences, the new wall shapes $y = b(x, t + \Delta t)$, $y = c(x, t + \Delta t)$ are updated by integrating Eqs. (14) and a new grid is determined according to the mapping (13). From geometrical considerations, as shown in Fig. 2, an alternative form of the time derivatives $\partial b/\partial t$ is

$$\frac{\partial b}{\partial t} = \frac{\widetilde{u}}{\cos\varphi} = \widetilde{u}\sqrt{1 + \left(\frac{\partial b}{\partial x}\right)^2} \tag{15}$$

which also applies to $\partial c/\partial t$.

The same inverse method can be used to determine the shape of plumes and interfaces. For instance, in flow regions such as after-bodies or dual nozzles in a bypass turbofan, contact surfaces are generated by the different stagnation conditions and thermodynamic properties of the incoming flows. These discontinuities are interfaces that can be computed explicitly according to the present inverse method. In the inviscid case they are considered as impermeable and deformable boundaries separating different flow regions, across which the pressure and the normal component of the flow velocity are imposed to be C^0 continuous and equal to the moving-boundary velocity.

The extension of the moving boundary condition to the viscous case follows the same guidelines of the boundary treatment for the direct problem solution. Once the wall impermeability is enforced by (15), which applies to both Euler and Navier–Stokes equations, appropriate physical boundary conditions as the slip/no-slip condition and a condition for the temperature field at boundary are imposed. Convective fluxes at boundary are evaluated as a wave signal propagation problem, i.e. a Riemann problem. At boundary one flow state is missing and unavailable signals

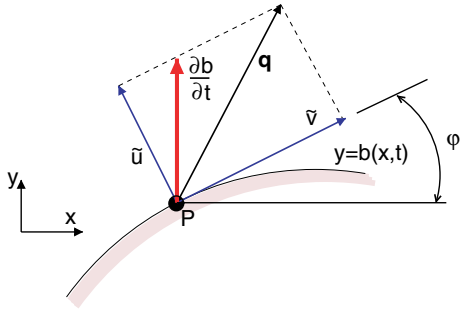

Fig. 2. Inverse problem: moving wall velocity.

are replaced by an equivalent number of boundary conditions, as requested for hyperbolic systems [23,25]. The differences rely therefore in the quality of the additional boundary conditions that one has to enforce. For instance, in the inviscid case one enforces the slip condition at walls, i.e. $\tilde{v} = \tilde{v}_{\text{inner}}$, being $\tilde{v}_{\text{inner}}$ the velocity component, tangential to the boundary, of the cell closest to the wall. Navier–Stokes equations requires the no-slip condition $\tilde{v} = 0$ at wall. In details, for isothermal walls, suitable BC are

$$\tilde{v} = 0, \quad T = T_{\text{w}} \tag{16}$$

while for adiabatic walls we impose

$$\tilde{v} = 0, \quad \frac{\partial T}{\partial n} = 0 \tag{17}$$

and, for the fitting of the previously mentioned contact surfaces

$$\tilde{v} = \tilde{v}_{\text{inner}}, \quad \frac{\partial T}{\partial n} = 0 \tag{18}$$

Relations (11), (15)–(18) are still valid in the axisymmetric case. The extension to the three-dimensional case follows the same guidelines given in this section. For instance, one can represent the unknown aerodynamic surface as a function $z = \beta(x, y, t)$ and enforce impermeability, obtaining formally again Eq. (10). In fact, the procedure explained here applies straightforward to 3D design at the cost of an unsteady Navier–Stokes computation.

2.2. Remarks on problem well-posedness

One drawback of inverse problems is that they may be ill-posed. If certain wall pressure distributions are required on airfoils, the result is an open or self-intersecting profile. Lighthill discovered the solvability conditions that have to be respected by pressure distributions within an incompressible potential flow model [6], whereas the similar integral conditions for compressible flows and other issues were investigated in Refs. [13,11,3,8]. These issues are typical of problem as airfoil or blade inverse design since they are related to the closure of the body contour. This problem has already investigated in the proposed literature and can be addressed in two ways: one can satisfy the closure conditions or reformulate the inverse problem in order to automatically satisfy such constraints [13].

As far as the design of two-dimensional duct is concerned, just some reasonable consideration on the acceptable pressure distribution are needed; for instance, the target pressure imposed at wall cannot be greater that the inlet total pressure.

The well-posedness problem in our approach is addressed with different attitude: we use "physical" time dependent technique and the problem is a well-posed problem from the point of view of the unsteady motion. As a matter of fact, we solve a mixed initial-and-boundary-value problem and we satisfy the requirements this kind of problem needs to be well-posed. If the design data we impose are violating the constraints needed by the "steady" well-posed problem, what we expect is that the computation will never reach a steady solution. Sometimes, the expected geometry is not obtained for a lack of problem uniqueness. More than one solution could be admissible for the same inverse problem and the numerical procedure is numerically triggered towards one of the

possible configurations. Often by changing a boundary condition the problem uniqueness is recovered [13].

3. Numerical results

With the aim of validating the viscous inverse solver and of focusing on its accuracy, few test cases were investigated. These tests consider some typical flow phenomena that occurs in simulating flowfields of practical interest of aerodynamic design, such as boundary layer or wakes treatment, shock–boundary layer interaction, strong expansion fans, etc. For validation purposes, the computed flowfields and shapes are compared with theoretical solutions or available experimental data.

3.1. Flat plate

The laminar flow over a flat plate is often used to validate viscous flow solvers because this flow problem has an analytical solution. The test case has been built up as follows: an initial, arbitrary shape of the lower boundary of the computational domain is selected, e.g. the solid curve labeled as (0) in Fig. 4, and a constant pressure distribution, the theoretical one, is imposed over it. The flat plate is $L = 5$ unit length wide, $-1 < x < 4$. Computational domain starts at $x = 0$ with an inlet velocity profile corresponding to the Blasius velocity solution at $Re = 10{,}000$ and the Reynolds number per unit length is $Re = 10{,}000$. A schematic view of the test-case configuration is given in Fig. 3. The free-stream Mach number has been chosen as ($M_{in} = 0.3$) to consider the flow as being approximately incompressible, while maintaining good convergence properties as far as a compressible flow solver is used. The adiabatic, viscous boundary conditions have been imposed. Nevertheless, the incompressibility approximation guarantees that the fluid dynamic field effectively remains independent of the temperature field.

The initial flowfield imposed does not match the target pressure at the wall, which starts moving to alleviate the pressure gap and to satisfy the viscous boundary conditions.

After a transient, whose duration depends on how far the initial configuration is from the final one, the system relaxes to a steady state that represents the target flowfield. The presented simulation uses 80×40 stretched grid to compute the flow. Fig. 4 shows the initial (0), two transient ((1), (2)), and the final shape (3) of the lower boundary of the computational domain, respectively. Curve (3) is the obtained, numerical approximation of the flat plate wall. Configuration (1) is

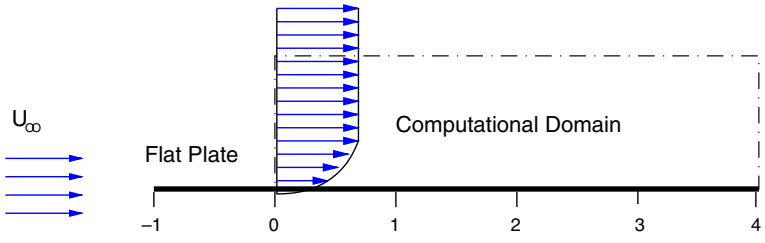

Fig. 3. Schematic view of the flat plate test-case.

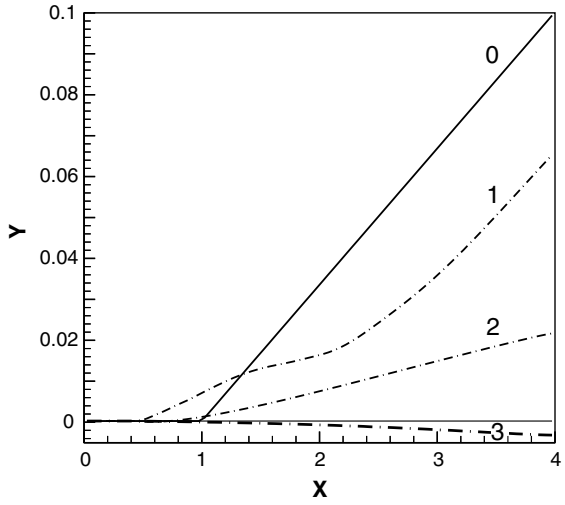

Fig. 4. Initial (0), transient (1), (2) and final (3) shape of the boundary contour, i.e. the plate itself, compared with the exact solution $Y = 0$. The same curve represents the local error in the boundary shape.

reached in 5×10^4 time steps, configuration (2) in 2×10^5 time steps, and the final geometry is obtained after 3×10^5 time steps. The computation takes about 1 h of CPU time on dual processor CompaQ DS20 workstation. At convergence the L^2-norm ρu residual is less than 10^{-8} and $(b_t)_{\max}/U_\infty \leqslant 10^{-6}$. Since the expected geometry is the straight line $y = 0$, line (3) of Fig. 4 also represents the absolute error in shape. As visible, the maximum absolute error ϵ occurs at the end of the flat plate is less than $\epsilon_m = 0.004$ unit length. The mean error along the moving part of the plate is then about 0.001. Common causes that explain the presence of such error are the accuracy of the discretization and integration scheme, and a slight, though non-zero, compressibility effect ($M_{in} = 0.3$). There is also an additional source of error due to the approximated treatment of the upper boundary. The convective fluxes on the upper boundary are extrapolated from the flow state at the last inner cells and the asymptotic conditions for $y \to \infty$, that is

$$u(\infty) = U_\infty, \quad v(\infty) = V_\infty = 0.8604 \cdot U_\infty \sqrt{\frac{\nu}{U_\infty x}}$$

The vertical velocity varies with Reynolds number and x-location, and it is known only for few simple flows. In general one set $v_\infty \simeq 0$, since it is very small as the Reynolds number increase. We used here this approximation even if the Reynolds number was not very high. Since the numerical method is conservative, the mass flow is preserved accurately. As a consequence the lower boundary find a steady configuration a little downward deflected to allow the discharging form the exit boundary of the mass not allowed to flow through the upper boundary. Accounting for the correct asymptotic conditions or by using non-reflecting boundary conditions we found a reduction of the shape error of about the 60%. Nevertheless the results obtained neglecting the vertical asymptotic velocity are in good agreement with the theoretical ones. Fig. 5 shows that the shape error is also very small if compared to the local boundary layer thickness δ and the

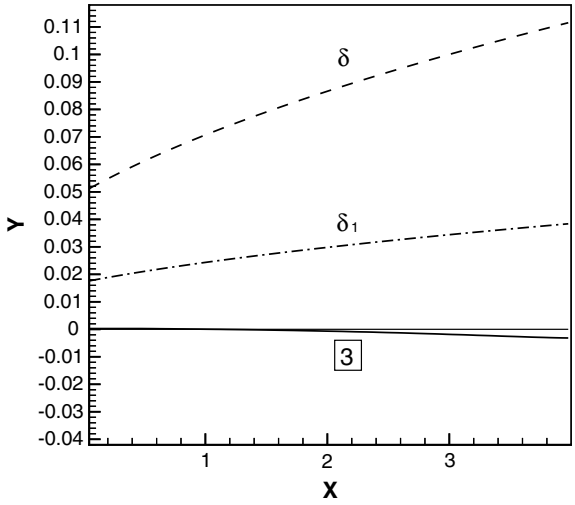

Fig. 5. Flat plate. Shape error (3) compared to the boundary layer thickness δ and boundary layer displacement thickness δ_1 along the plate.

displacement thickness δ_1. Moreover, the computed velocity profile well matches the corresponding Blasius solution, as shown in Fig. 6.

3.2. Laminar wake

An inverse problem can be formulated not only to obtain the shape of the wall that realizes a prescribed pressure distribution over it, but also to fit contact surfaces that separate two

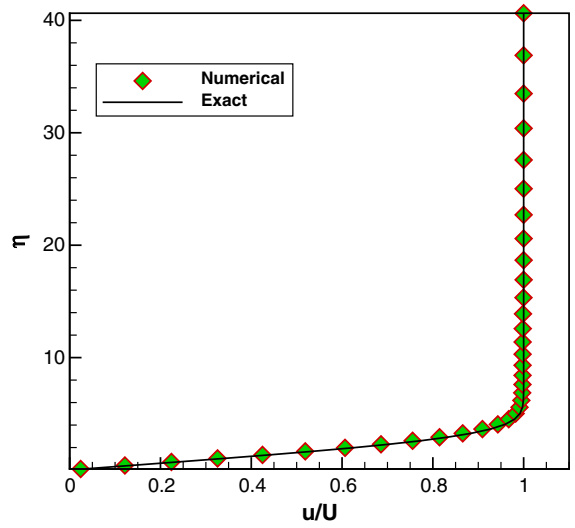

Fig. 6. Flat plate. Velocity profile at $x/L = 3.5$ compared with the Blasius solution.

co-flowing streams with different thermodynamic properties. In the inviscid case this corresponds to concentrating the shear layers between the two streams by an ideal slip surface. The shape of such a surface is unknown a priori and is derived as part of the final solution of an inverse problem, as described in Ref. [18]. In the same work it has been shown that this approach is superior to using capturing techniques for such contact discontinuities, since it does not suffer from numerical diffusion problems. The result is an almost grid independent solution and an accurate treatment of shock reflections over the contact discontinuity. A laminar wake can be seen as an enhancement of the previously mentioned shear layer model. From the applicative point of view, the fitting of viscous slip surfaces is of interest because it allows the interaction between the aerodynamic body and the external flow to be directly included in the design problem. One can, for example, design the nozzle contour that realizes a given expansion ratio and also some specified adaptation characteristics at the cruise condition.

In the present test case we formulate an inverse problem that has, as objective flowfield, the laminar wake behind a flat plate for which an analytic solution of the asymptotic velocity profiles is given by Schlichting [26]. A schematic representation of the computational domain is given in Fig. 7. A constant pressure distribution $p_{\text{wall}}(x) = 0.9395$ along the wake centerline has been imposed. The lower boundary of the computational domain is considered partly the solid wall of the flat plate and partly a viscous slip surface. The inverse problem follows the guidelines of the previous test: an arbitrary initial geometry is guessed for the wake centerline and the pressure distribution is enforced. The imposed boundary conditions are

$$p = p_{\text{wall}}(x), \quad \tilde{u} = 0, \quad \tilde{v} = \tilde{v}_{\text{inner}}, \quad \frac{\partial T}{\partial n} = 0 \tag{19}$$

The evolution of the boundary surface is qualitatively similar to the previous cases. The main difference is that now the final shape of the lower boundary corresponds to the wake centerline instead of representing the final wall contour. The initial and final geometry of this surface are shown in Fig. 8a. As observed in the first test case proposed, i.e. the Blasius solution, the shape error per unit of length is about constant, $\epsilon_{\text{m}} \simeq 0.001$. The computed axial velocity profile at $x/L = 5$ is compared in Fig. 8b to the asymptotic solution given by Schlichting [26]

$$\frac{U_\infty - u(x,y)}{U_\infty} = \frac{0.664}{\sqrt{\pi}} \left(\frac{x}{L}\right)^{-\frac{1}{2}} \exp\left(-\frac{1}{4}\frac{y^2 U_\infty}{vx}\right) \tag{20}$$

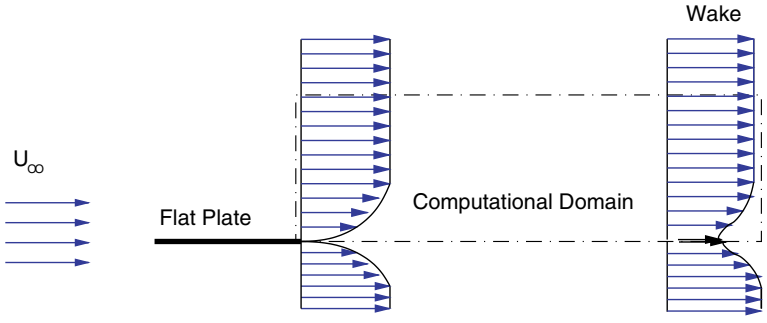

Fig. 7. Schematic view of the laminar wake test-case.

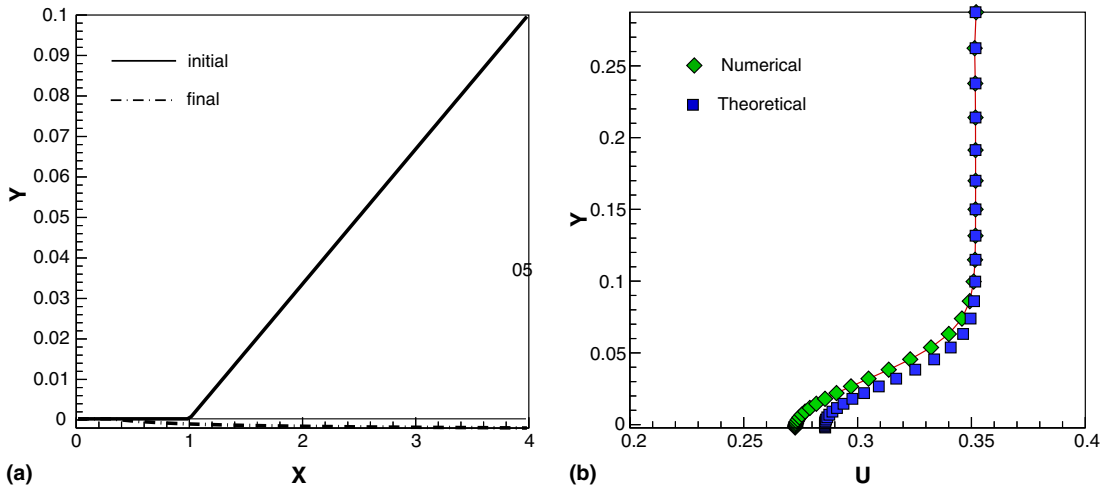

Fig. 8. Laminar wake test-case. (a) Wake centerline geometry, (b) axial velocity profiles.

The slip velocity on the surface is underestimated by about the 5%. Nevertheless, this error does not affect the accuracy of the final geometry.

3.3. Supersonic ramp

The supersonic corner flow is a fundamental problem that has been studied extensively to investigate complex phenomena related to the shock–boundary layer interaction. From the engineering point of view, compression corners and ramps are the preferred devices used to decrease total pressure losses in supersonic air intakes by originating favourable shock patterns. In the present test case, the target flowfield corresponds to the $M_\infty = 2.85$ viscous flow over two-dimensional compression corner of 16° angle. Fig. 9 shows the initial computational domain. The numerical solution has been computed on a 100×50 stretched grid. The upper boundary of the computational domain has been chosen to avoid any interference between the shock originated at the corner and the boundary itself. The Reynolds number is 10^5. The initial condition is an uniform flowfield at $M = 2.85$.

The target pressure distribution imposed on the moving wall is obtained from the direct simulation of Navier–Stokes equations at the corresponding ramp angle. Fig. 13 shows the final corner geometry and the Mach number contour lines. Target and computed pressure distributions and wall shapes are compared in Figs. 10 and 11, respectively. We remark that the pressure distributions are indistinguishable while the computed ramp geometry is approximable as a straight line. The geometry accuracy could be evaluated simply as a difference between target and computed ramp angle. Table 1 reports the imposed and obtained ramps for four different angles. The maximum relative error is very small, about 1%. The convergence history of the L^2-norm of ρu-residual is plotted in Fig. 12.

Although the present implementation of the inverse solver assumes the flow to be laminar, a comparison with experimental (turbulent) data [27] can give more information on the level of

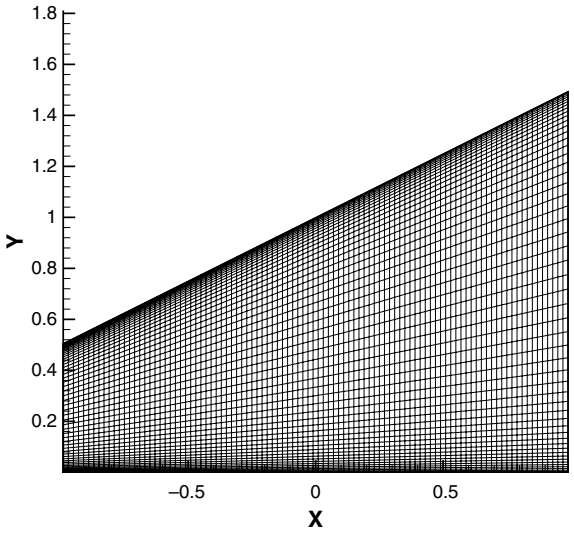

Fig. 9. Supersonic ramp. Initial geometry.

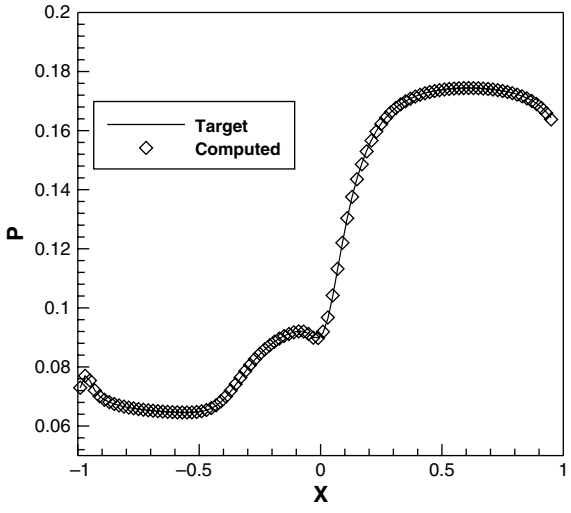

Fig. 10. Supersonic ramp. Target and computed wall pressure distribution.

approximation obtained by the numerical simulations. A comparison of the wall pressure distributions for three different ramp angles (8°, 16° and 20°) is shown in Fig. 14. The wall pressure and the x abscissa are normalized by the ambient pressure P_∞ and the boundary-layer thickness at the corner position δ_0, respectively. Numerical simulations, due to the laminar flow approximation, incorrectly capture the dimensions of the recirculating bubble. Nevertheless, from Fig. 14 it is shown that this effect is confined in a region smaller than $4\delta_0$ wide. Outside this region the wall pressure distribution are in good agreement.

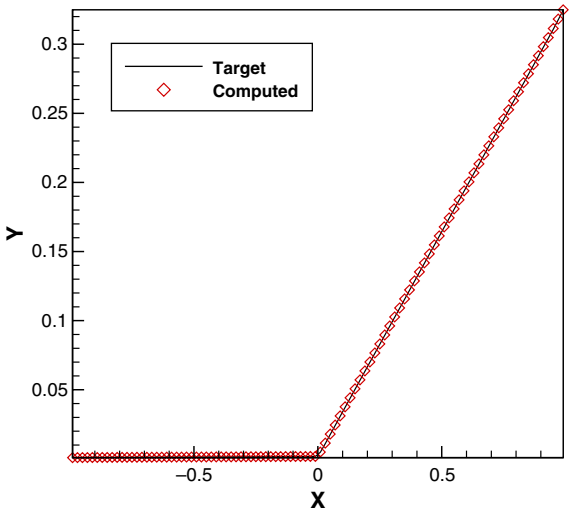

Fig. 11. Supersonic ramp. Target and computed wall geometry.

Table 1
Supersonic ramp. Comparison between the numerical and experimental ramp angle

Mach number	Exp. ramp angle	Comp. ramp angle
2.85	8°	8.07°
2.85	14°	14.10°
2.85	16°	16.01°
2.85	20°	20.21°

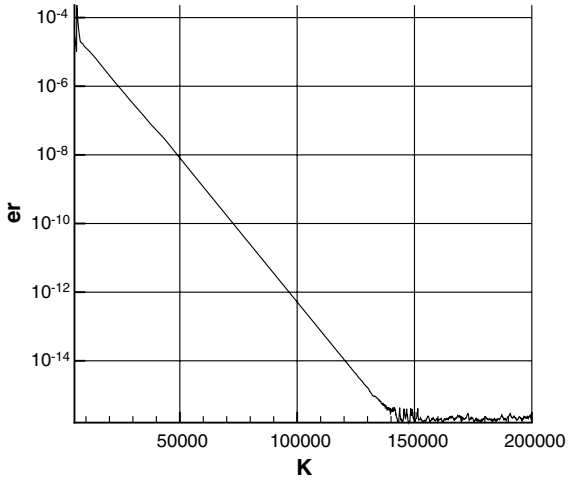

Fig. 12. Supersonic ramp. Convergence history.

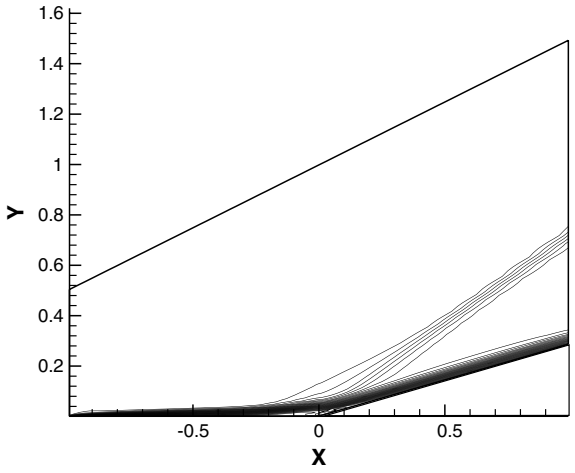

Fig. 13. Supersonic ramp. Mach number contour lines.

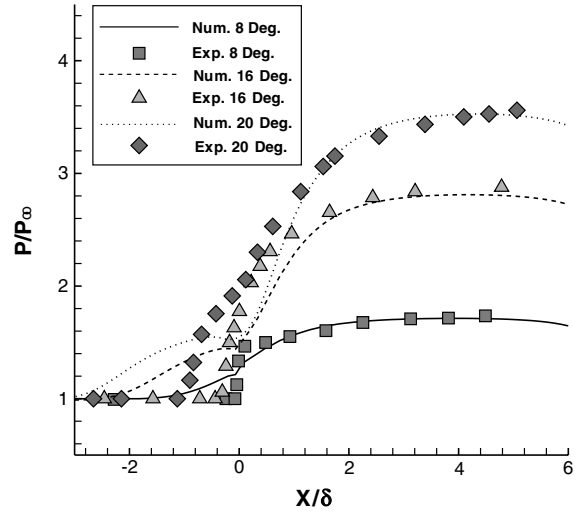

Fig. 14. Supersonic ramp. Pressure comparison between numerical and experimental data.

3.4. Linear plug nozzle

The plug nozzle design should be considered a severe test, since it involves a rapidly expanding, transonic-to-supersonic flow. Any geometrical modification has a great influence on the whole flowfield and can cause the formation of shocks, which lead abruptly the system to a completely different flow pattern. Following Angelino's method [28], an ideal contour of the plug has been defined, which will hereafter be called the *target plug contour*. We set the design pressure ratio PR = 200. The outcoming jet is expanding in a quiescent flow. Reference flow conditions are taken from experiments within the FESTIP Research Program (plug LNP1) [29], where

performances of truncated plugs, also called aerospikes, are compared to the ideal behaviour of the full length nozzle. The Reynolds number, based on the plug length, was set at $Re = 10^7$, a value which is in the range of practical applications. Regardless of the Reynolds number, as for the previous tests, the flow is assumed to be laminar. Again, to set up the test case, for the given plug geometry, the wall pressure is computed using a direct Navier–Stokes flow solver. This pressure distribution is then enforced as the target pressure at the plug wall and the inverse problem is solved for the nozzle geometry. No matter what the initial condition is, we expect the final geometry to accurately replicate the target plug contour. The numerical test was solved on a 100×52 grid. Stretching was used in the y-direction, to better refine the region close to the upper and lower boundaries, and also in the x-direction, to cluster points in the region where most of the expansion takes place.

The upper boundary is implemented as a far-field condition, while the bottom boundary moves according to the procedure of inverse designing. A sequence of the flowfield evolution during the transient is presented in Fig. 15. The starting geometry is visible in Fig. 15a. The target flow solution is characterized by a continuous expansion, without discontinuities, while the presence of a

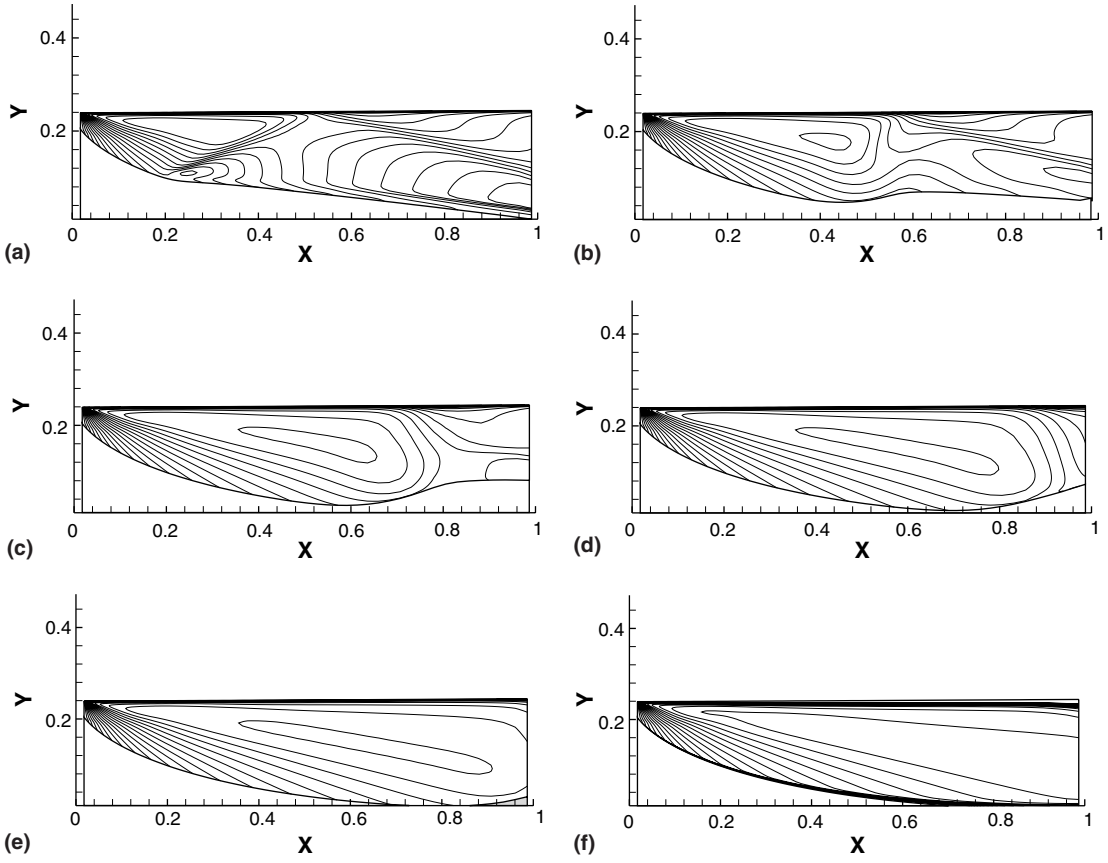

Fig. 15. Inverse problem on a plug nozzle. Snapshots of the evolving flowfield in terms of Mach number isocontours. (a) Initial, (b–e) intermediate, (f) final flowfield.

shock and its reflection are quite visible in the initial flowfield. The initial flowfield can therefore be considered sufficiently far from the target one. The inverse problem procedure is in fact driven by flow evolution, so that the complexity of the initial flowfield, rather than the initial geometry of the domain, is of relevance. A typical evolution of the boundary subjected to conditions (15) and (16) or (17) dictated by the inverse procedure is also visible in Fig. 15. After a motion that somehow resembles a "whip lash", the contour assesses to the imposed boundary pressure, and a microscopic motion, on the scale of the boundary-layer thickness, takes place to balance the viscous fluxes in the proximity of the wall. The plug shape is obtained with high accuracy. In Fig. 16 the target and the computed geometry are indistinguishable. An expected result is the good agreement between the imposed and the obtained wall pressure distribution, as confirmed by the grid refinement study in Fig. 18. The design of a plug nozzle, due to its non-banal geometry, is in fact a good candidate to performing a grid refinement study. The computed geometry and wall pressure distributions are obtained on three different grid sizes 50×30, 100×52, 150×80, respectively. The results confirm that the methodology is independent of the grid size and a logarithmic scaling is necessary in Fig. 18 to highlight minimal discrepancies between the target and computed plug contours. The highest mismatch is observed in the proximity of the spike end, the relative error in the plug geometry being of the order of 10^{-3} for the coarsest grid (50×30 cells). The geometrical differences between the solution of the viscous and inviscid inverse problem are shown in Fig. 17. From a practical point of view, the test-case seems to be almost inviscid and one could account for viscous effects efficiently by evaluating the boundary layer blockage by using a viscous–inviscid coupling technique. The added value of the proposed methodology is the higher confidence that the resulting plug geometry realizes a steady flowfield that does not suffer of unwanted laminar separations and periodic flow fluctuations. This key feature is of relevance when flow quality control is required, as, for instance, in rocket nozzle design. In this case any kind of unsteadiness that can lead to significant side-loads must be avoided, as they are a major cause of uncontrolled motions and mission failure.

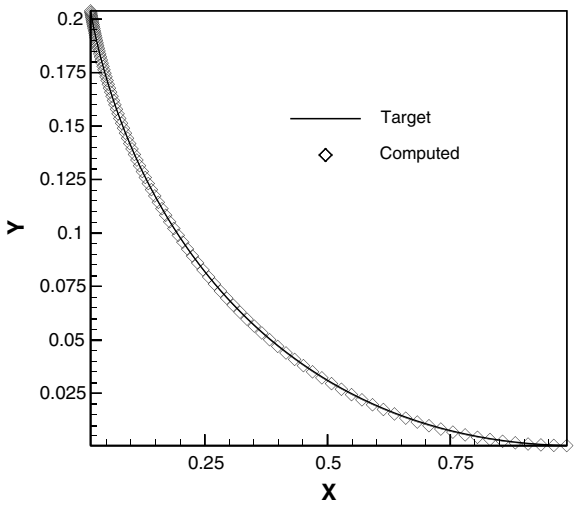

Fig. 16. Comparison between computed and target plug nozzle.

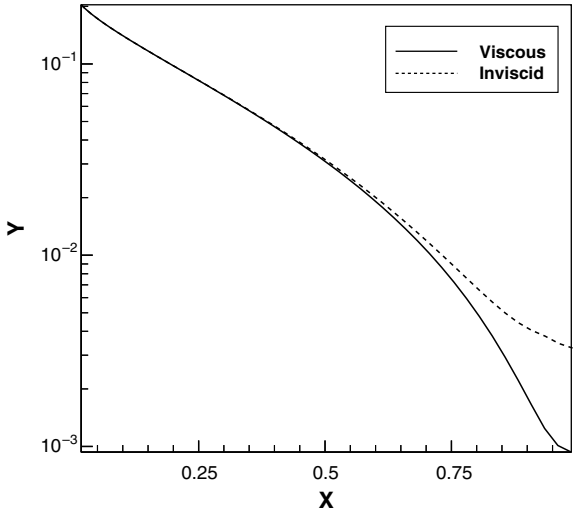

Fig. 17. Viscous versus inviscid inverse solution.

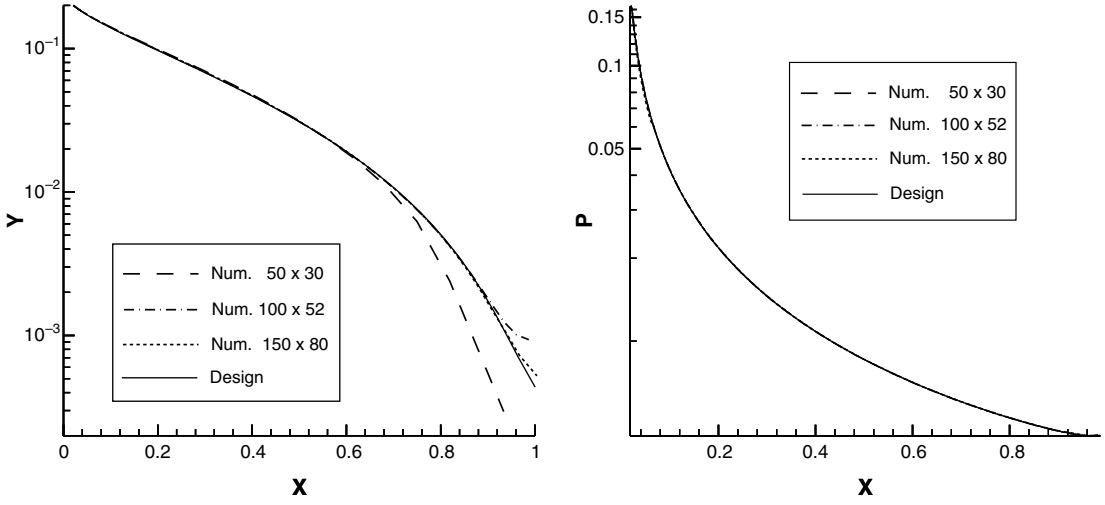

Fig. 18. Plug nozzle. Plug geometry (left) and pressure distribution (right) comparisons for different grids.

3.5. Dual bell nozzle

The last example refers to the design of an axisymmetric dual bell nozzle. This nozzle concept is of actual interest for its unique feature of a one-step altitude adaptation, achieved only by a wall inflection and, thus, without moving parts. At low altitudes, controlled and symmetrical flow separation occurs at the wall inflection, which results in a smaller effective area ratio without generating dangerous side loads. At higher altitudes, the nozzle flow is attached to the wall until the exit plane and the full ratio is used. Because of the higher area ratio, an increase in vacuum

performance is achieved. The overall design parameters are kept from Hagemann et al. [30] and refer to the truncated ideal base nozzle and a nozzle extension with favourable wall pressure gradient (TICNP).

The numerical tests was solved on a 100×52 stretched grid. The initial configuration has been arbitrarily chosen as the supersonic flowfield in a constant duct, with the Mach number linearly varying from $M_{in} = 1$ to $M_{ou} = 3$. The pressure distribution imposed on the upper boundary is a spline fitting of the experimental data given in Ref. [30] (with symbol –▷– in Fig. 21) and refers to the case of adapted nozzle. The design pressure ratio PR = p_c/p_a is set to 200, where p_c and p_a are the chamber and ambient pressure, respectively. The Reynolds number, based on the throat radius r_{throat} is $Re = 2 \times 10^5$. The nozzle length is $L/r_{throat} = 17$. A sequence of the flowfield evolution during the transient is presented in Fig. 19. Pressure contour lines are also showed in the same figure. The evolution of the moving grid is shown in Fig. 20. Wall pressure data p_w/p_c computed by the inverse method (**cpf**) (dotted line) are compared with the experimental results (**epf**) (right triangles) are shown in Fig. 21. Since the exact nozzle geometry was not given in Ref. [30], an alternative way of validation has been sought. To put on evidence the correctness of the results,

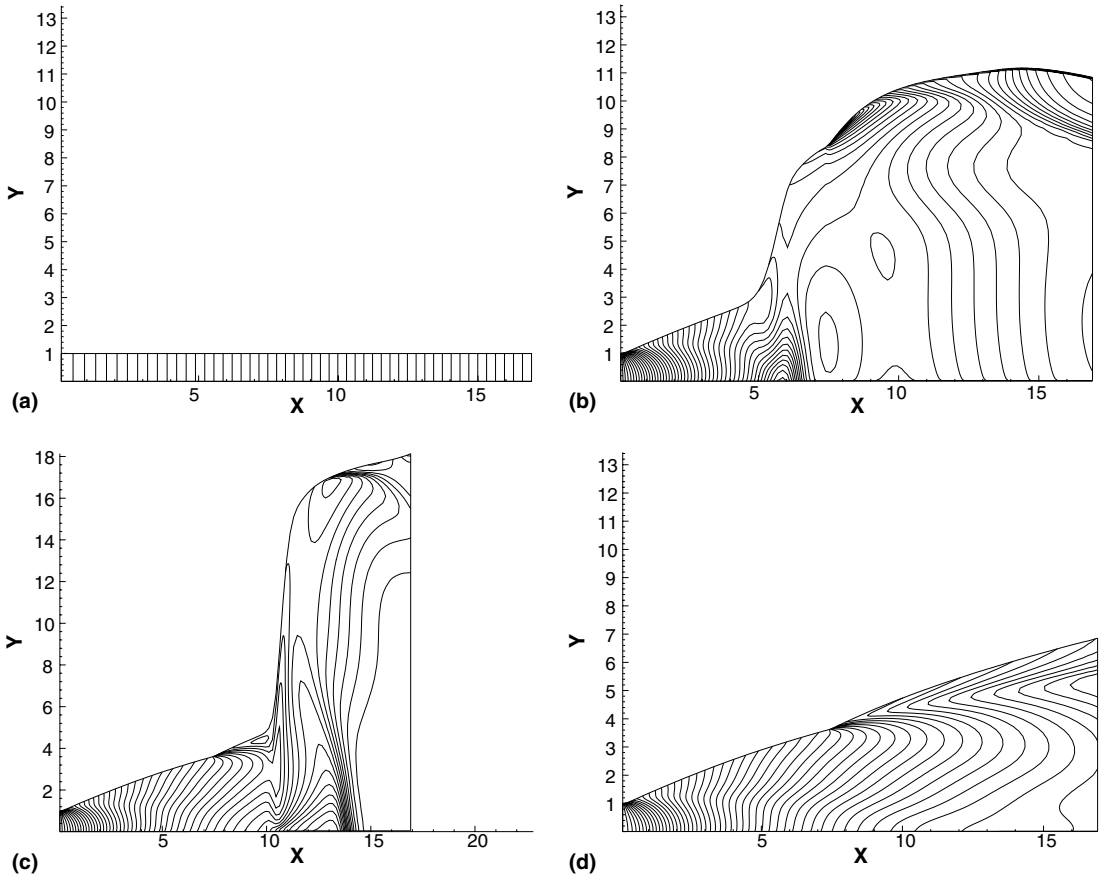

Fig. 19. Dual bell nozzle. Flowfield evolution: (a) initial; (b) and (c) transient (d); final configuration.

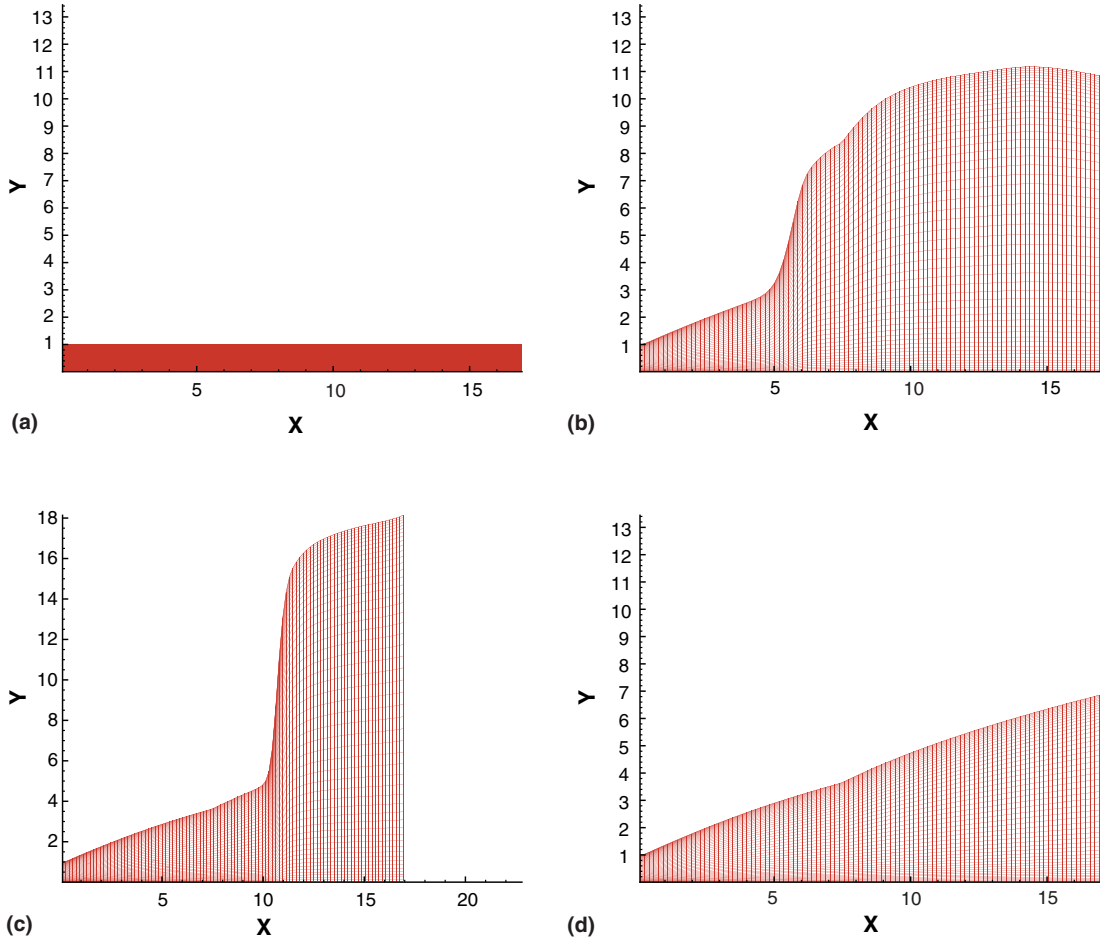

Fig. 20. Dual bell nozzle. Grid evolution: (a) initial; (b) and (c) transient; (d) final configuration.

the computed shape has been fixed and some off-design conditions of the nozzle are investigated by a direct, laminar solver. The off-design pressure data are ranging between $30 \leqslant \mathrm{PR} \leqslant 50$. A reasonable agreement between the numerical and experimental pressure distributions is shown in Fig. 21.

4. Conclusions

A viscous, inverse solver based on Navier–Stokes equations has been proposed and validated through theoretical and experimental test-cases. This approach, which essentially tracks a unsteady flow surface until a steady configuration is reached, extends to viscous flows a well-established procedure for Euler equations. The additional boundary conditions, required for a correct boundary treatment in viscous flows, are introduced in the original technique in the same way as for the

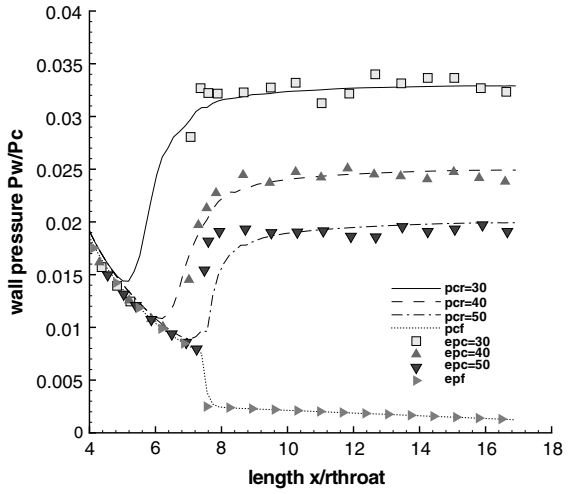

Fig. 21. Dual bell nozzle. Wall pressure comparison.

"direct problem" solution. The tests have shown that the technique gives an accurate representation of the target flowfield geometry and of the flow solution, in the limit of a laminar approximation. Since only the steady configuration is of interest, the procedure could be greatly enhanced using over-relaxing techniques. Some remarks on well posedness has be given. The case of airfoil and blade design is avoided intentionally, since inverse problem formulation and the related issues on problem uniqueness merit a separate investigation. The extension to three-dimensional flows is straightforward, at the cost of a fully unsteady viscous flowfield evaluation.

References

[1] Jameson A, Martinelli L, Pierce NA. Optimum aerodynamic design using the Navier–Stokes equations. Theor Comput Fluid Dyn 1998;10:213–37.
[2] Iollo A, Ferlauto M, Zannetti L. An aerodynamic optimization method based on the inverse problem adjoint equations. J Comput Phys 2001;173:87–115.
[3] Volpe G. Inverse airfoil design: a classical approach updated for transonic applications. Appl Comput Aerodyn 1990;125:191–220.
[4] Patrick SM, Atassi HM, Blake WK. Inverse problems in aerodynamics and aeroacoustics. Active Control Vib Noise, ASME 1994:309–19.
[5] Mangler W. Die berechnung eines tragflügelprofiles mit vorschriebener drückverteilung. Jahrb Deut Luftfahrtvorschung 1938;1:46–53.
[6] Lighthill JM. A new method of two-dimensional aerodynamic design. Aeronautical Research Council Reports and Memoranda n. 2122, 1945.
[7] Staniz JD. Design of two-dimensional channels with prescribed velocity distributions along the channel walls. NACA Report 1153, 1953.
[8] Daripa P. Solvability condition and its application to fast numerical solution of overposed problems in compressible flows. J Comput Phys 1991;95:436–49.
[9] Zangeneh M. Inviscid–viscous interaction method for 3d inverse design of centrifugal impellers. ASME J Turbomach 1994;116:280–90.

[10] Elizarov AM, Il'innskiy NB, Potashev AV. Mathematical methods of airfoil design. Berlin: Akademie Verlag; 1997.
[11] Volpe G. Geometric and surface pressure restrictions in airfoil design. AGARD Rep. n. 780, 1990.
[12] Zannetti L. Time dependent method to solve inverse problems for internal flows. AIAA J 1980;18:754–8.
[13] Zannetti L, Pandolfi M. Inverse design techniques for cascades. NASA CR 3836, 1984.
[14] Malone JB, Vadiak J, Sankar LN. A technique for inverse aerodynamic design of nacelles and wing configurations. J Aircraft 1987;24(1):8–9.
[15] Demeulenaere A, Van den Braembussche R. Three-dimensional inverse method for turbomachinery blading design. ASME J Turbomach 1998;120(1):247–55.
[16] Zannetti L, Larocca F, Marsilio R. Euler solver for 3d inverse problems. In: Baysal O, editor, Advances and Applications in CFD, vol. 66, 1988. p. 71–9.
[17] Ferlauto M. Aerodynamic design via inverse problem solution in three-dimensional incompressible flows. GIMC-AMC 2002 Joint Conference, Giulianova, Italy, 2002.
[18] Ferlauto M, Larocca F, Zannetti L. Integrated design and analysis of intakes and nozzles in air-breathing engines. J Propul Power 2002;18:28–34.
[19] Wilhelm R. Inverse design method for designing isolated and wing-mounted engine nacelles. J Aircraft 2002;39(6):989–95.
[20] De Vito L, Van den Braembussche R, Deconinck H. A novel two-dimensional viscous inverse design method for turbomachinery blading design. ASME J Turbomach 2003;125(2):310–6.
[21] Dulikravich GS. A criteria for surface pressure specification in aerodynamic shape design. AIAA paper 90-0124, Reno, NV, 1990.
[22] Marsilio R. Numerical simulations for plug nozzle flowfields. AIAA Paper 2001-0670, 2001.
[23] Pandolfi M. A contribution to the numerical prediction of unsteady flows. AIAA J 1983;22:37–46.
[24] Harten A, Engquist B, Osher S. Uniformly high-order accurate essentially non-oscillatory schemes III. J Comput Phys 1987;71:231–303.
[25] Poinsot TJ, Lele SK. Boundary conditions for direct simulations of compressible viscous reacting flows. J Comput Phys 1992;101:104–29.
[26] Schlichting H. Boundary-layer theory. New York: McGraw-Hill; 1979.
[27] Settles GS, Fitzpatrick TJ, Bogdonoff SM. Detailed study of attached and separated compression corner flowfields in high Reynold number supersonic flow. AIAA J 1979;17:579–85.
[28] Angelino G. Approximate method for plug nozzle design. AIAA J 1964;2(10):834–5.
[29] Immisch F, Terhard H. Advanced nozzle activities at DASA. In: Proc. ESA-ESTEC Advanced Nozzles Workshop, Rome, Italy, 1997.
[30] Hagemann G, Terhardt M, Haeseler D. Experimental and analytical design verification of the dual-bell concept. J Propul Power 2002;18:116–22.